Inversão para CSEM marinho empregando derivadas analíticas

Aluno: **João Lucas Silva Crepaldi**
Orientador: **Irineu Figueiredo**
Co-orientador: **Marco Polo Buonora**

Dissertação apresentada ao Observatório Nacional do Rio de Janeiro como requisito parcial à obtenção do título de MESTRE em Geofísica.

Livros Grátis

"INVERSÃO PARA CSEM MARINHO EMPREGANDO DERIVADAS ANALÍTICAS"

JOÃO LUCAS SILVA CREPALDI

DISSERTAÇÃO SUBMETIDA AO CORPO DOCENTE DO PROGRAMA DE PÓS-GRADUAÇÃO EM GEOFÍSICA DO OBSERVATÓRIO NACIONAL COMO PARTE DOS REQUISITOS NECESSÁRIOS PARA A OBTENÇÃO DO GRAU DE MESTRE EM GEOFÍSICA.
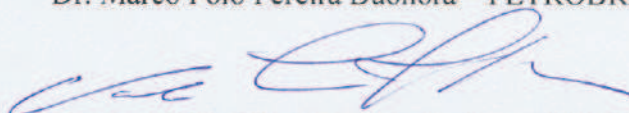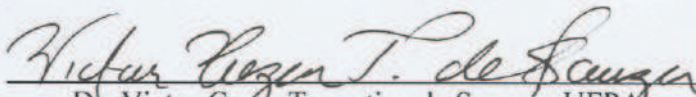
Aprovada por:

_____
Dr. Irineu Figueiredo – ON/MCT

_____
Dr. Marco Polo Pereira Buonora – PETROBRAS

_____
Dra. Valéria Cristina Ferreira Barbosa – ON/MCT

_____
Dr. Victor Cezar Tocantins de Souza – UFPA

RIO DE JANEIRO - BRASIL
17 DE SETEMBRO 2010

"...porque a beleza da geofísica de exploração é iluminar a Terra com uma luz que não se pode ver, para torná-la visível!."

Resumo

O *marine controlled-source electromagnetic method* (mCSEM) vem sendo crescentemente empregado pela indústria de hidrocarbonetos na redução de riscos exploratórios, entretanto a interpretação destes dados ainda é um desafio para a indústria petrolífera. Metodologias diretas de geração de perfis ou mapas de anomalia, assim como inversões 1D simples, se mostram insatisfatórias, por outro lado, algoritmos de inversão 2D e 3D requerem implementação complexa e altos custos computacionais.

Este trabalho apresenta todos os módulos de um fluxo de inversão mCSEM, que inverte o dado no domínio do *common mid-point* (CMP), como um conjunto de modelos 1D correspondentes às respectivas células CMP. Incluindo as derivadas analíticas das respostas para modelos 1D, em relação às resistividades das camadas, que além de tornar a inversão dezena de vezes mais rápida, pode ser útil ao entendimento de alguns aspectos do problema eletromagnético.

Estas técnicas foram aplicadas tanto a dados sintéticos como de campo, recuperando em poucos minutos seções geoelétricas com o corpo resistivo em sua posição correta assim como uma boa estimativa das resistividades *background*. Tais resultados provaram esta rotina, como ferramenta útil à interpretação exploratória.

Sumário

Fast marine CSEM inversion using analytical derivatives

João Lucas Crepaldi[12] and Marco Polo Buonora[1] and Irineu Figueiredo[2]

ABSTRACT

The employment of marine controlled-source electromagnetic method (mCSEM) to reduce risks in the exploration of hydrocarbons has being gradually growing, however the interpretation of the rendered data is still a challenge for the oil industry. Methodologies for generating profiles or maps of anomaly are often unsatisfactory as well as purely 1D inversion, on the other hand, the algorithms of 2D and 3D inversion require complex implementation and high computational costs.

This work presents the needed parts to implement a work-flow of mCSEM inversion, that inverts the data in common mid-point (CMP) domain, as a set of 1D models which correspond to their respective CMP cells. Including the analytical derivatives of the responses for 1D models, with respect to the resistivities, which apart from making the inversion tens times faster, it can be useful to clarify some features of the electromagnetic problem.

These techniques were applied to synthetic and field data, recovering in a few minutes geoelectrical sections with the resistive body at correct position and well estimated background resistivities. Such results proved this routine, as useful tool for exploratory interpretation.

INTRODUCTION

Marine controlled-source electromagnetic method (mCSEM) has been recently established as a technique for hydrocarbon exploration, mainly because of the high sensitivity to thin resistive layers (Constable and Weiss, 2006), due to the particular geometry of the fields produced by the horizontal electric dipole (HED), which generates transverse electric and magnetic modes of propagation (TE and TM), with respect to horizontal stratification (Nabighian, 1987). The TM mode has special interaction with horizontal interfaces of resistivity, building up charge density in this surface, on the other hand, TE mode is less sensitive, because it contains only the contribution of inductive effects, for this kind of feature (Um and Alumbaugh, 2007; Christensen and Dodds, 2007). Generally associated with seismic data and resistivity well log, georesistivity information provided by mCSEM can reduce significantly exploratory risks (Eidesmo et al., 2003).

The recent history in exploration as well as the complexity of fields generated by HED in marine environments, leads to a great demand of processing and inversion algorithms for the petroleum industry. One simple way to interpret the mCSEM data is setting the amplitude of the electric (E) and magnetic (H) fields in common offset domain and plot the data points at the common mid-point (CMP) position (between source and receiver coordinates), providing profiles or maps of anomaly. Background models based on seismic, resistivity well log, or even magnetotelluric information, could reduce the effects due to the presence

of complexities in geoelectrical background, through the normalization of the data by the modeled background response. However, since the effects of these causative structures are nonlinear, even with well approximated background information, this normalization may be insufficient to provide reliable results for the interpretation of the anomaly.

Moreover, it is difficult, or almost impossible to estimate the depth, resistivity and thickness of the target, because these parameters are complexly related to the offsets and frequencies involved. Thus, the most likely technique to interpret this signal should be the inversion by minimizing the L_2-norm of residual between data and estimated model response (Zdhanov, 2001).

There are a few softwares for 2D and 3D inversions of mCSEM data, and the forward solution which they employ are based on three basic discretization methodologies: finite differences, finite elements and integral equation. Generally, the implementation of these methodologies employs approximations, which are more or less suitable for each geological environment (Vdeev, 2005). Furthermore, the computation of these inversion programs could be very expensive and slow to exploratory needs. The purpose of this work is to present the development of an inversion for mCSEM data by minimizing the L_2-norm of residual between measured data, in CMP domain, and the modeled HED responses for a set of 1D models, corresponding to CMP cells in the cross-section (Mittet et al., 2008). As all 1D models are inverted simultaneously, at the same vector of parameters, it is possible to laterally constrain the layers, adding stability to the inversion and enables to introduce geological information about the lateral continuity of layers (Auken and Christiansen, 2004).

The data were inverted in CMP domain, because the data of several source-receiver pairs whose mid-points belong to a given CMP cell are more sensitive to the same horizontal region of subsurface if it is quasi-layered medium. So for an approximated 1D background, the recovered resistivity of a body should be more close to real, as the body shape approximates to an extensive plane layer, for a given depth, thickness, width of CMP cell, frequency and offsets involved.

The methodology was then successfully applied to an mCSEM line named LTAM10 of a survey in Santos Basin (Buonora et al., 2008), but first, a work-flow of inversion was tested in synthetic data of a 3D model similar to the geological frame of the section corresponding to LTAM10 and its surroundings, interpreted from seismic and resistivity well log information.

In addition, this paper presents the analytical derivatives of the 1D HED responses with respect to the resistivities of layers, which turns the inversion up to forty times faster than the same algorithm employing numerical derivatives, increasing speed and sensitivity for each iteration.

METHODOLOGY

All parts involved in the inversion work-flow are discussed in this section: the forward responses for HED in a layered model, the CMP transformation, the model discretization, the inversion algorithm and the derivative calculus of these responses with respect to the layer resistivities.

Forward mCSEM1D

The 1D HED forward code employs the fields equations deduced in Tocantins (2007), from Schelkunoff potentials approach (Nabighian, 1987). As these equations will be used in analytical derivatives calculation, they are completely formulated in Appendix A.

Because of the symmetry of 1D earth around to z-axis, the inverse transformation of the fields, from wave numbers to spatial domain are expressed in terms of Hankel transforms (Nabighian, 1987). Since the refflection coefficients are intrincate functions of the wave number, there are no known analytical solutions for the integrals in Appendix A, so a way to solve them is through digital filters (Guptasarma and Singh, 1997).

In order to optimize the forward code, the $|E_x|$ (0.75 Hz) responses for 1-Ωm-whole-space were generated, using the digital filters with 61, 120, 241 of Kong (2007), and 201 and 400 points employed in Key (2009); and then compared with the analytical solution for a dipole at the same model (Nabighian, 1987), (see Figure 1).
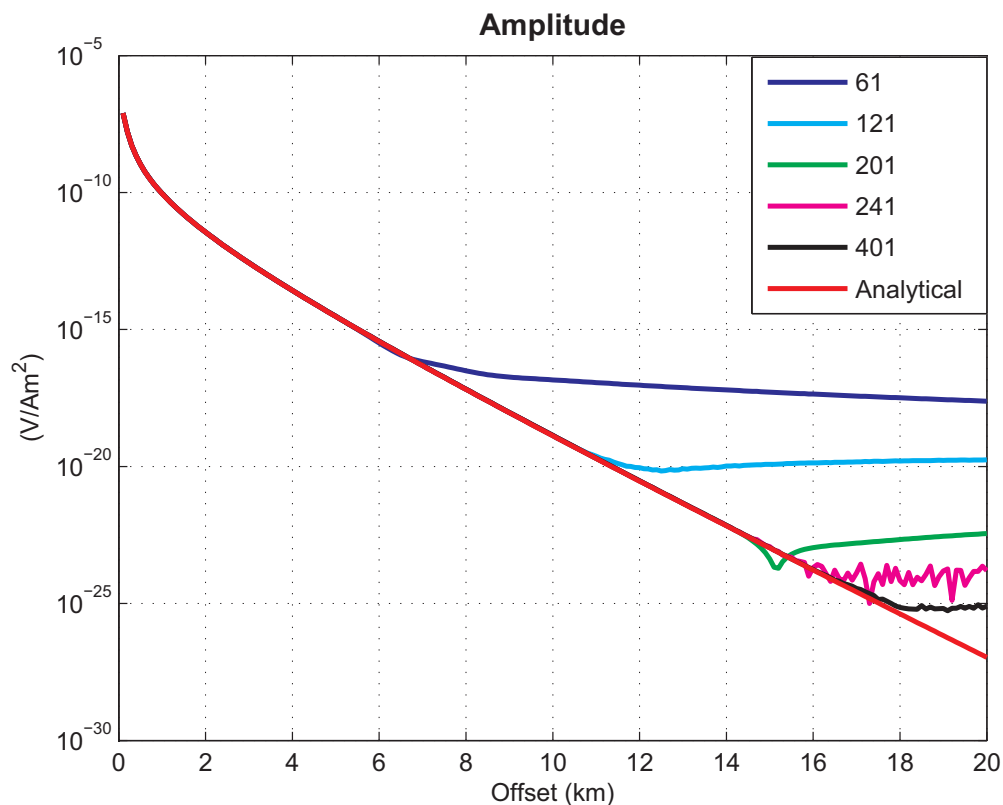
Figure 1

Figure 1: The $|E_x|$ (0.75 Hz) responses for 1-Ωm-whole-space model, employing digital filters of 61, 121, 201, 241 and 401 points, are compared with the analytical solution for this model.

Figure 1 sows that the responses of all filters are closer to being analytical, until the noise threshold of 10^{-15}V/Am^2, in this case the threshold occurs around 5.5-km-offset. However it is prudent to employ a filter that can well solve longer offsets, because in stratified models

the numerical error could be greater.

Based on these assumptions and in a compromise between number of points and accuracy, the filter Kong-241-points was chosen.

CMP domain

In order to analyze the CMP data, a 3D synthetic model in Figure 2 was generated based on an interpretative cross-section and survey parameters of the profile LTAM10, which will be detailed in the Field Data section. The $E_x(0.75Hz)$ responses was then computed for all 11-receivers, using a forward modeling, based on Integral Equation (Zdhanov, 2009).
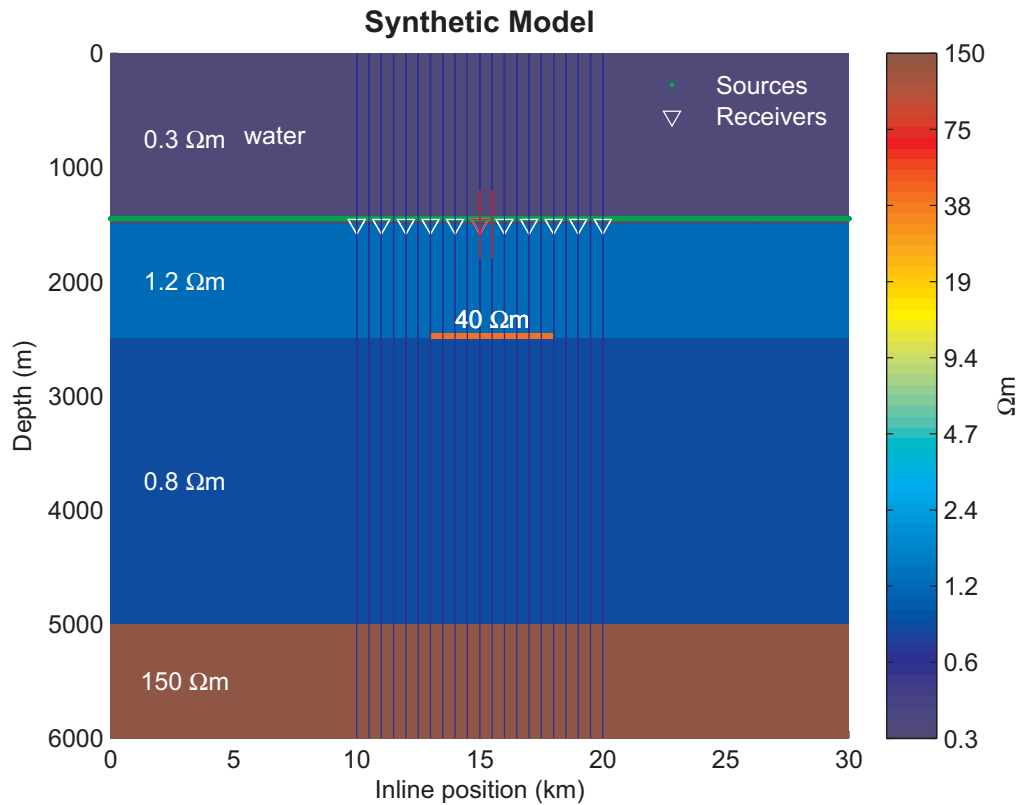
Figure 2

Figure 2: This synthetic geoelectric model is similar to the geoelectrical frame of mCSEM line LTAM10. The resistive body has a thickness of 50 m and extension in y-direction (normal to the page) of 20 km, which is a well 2D body approximation for the frequencies involved. The positions and resistivity are in accordance with the seismic and resistivity well log information. The 150-Ωm-bottom layer is the half-space basement. The receivers and sources are 1 km and 100 m apart, respectively; the sources are towed 50 m above sea-bottom. The blue vertical lines are CMP cells discretization. The red lines indicate CMP-11 and the red triangle denotes the receiver-6 .

The transformations of the signal position from source x_s and receiver x_r coordinates,

to CMP x_c and offset x_h coordinates, are given by:

$$x_c = \frac{1}{2}(x_s + x_r),$$
$$x_h = (x_s - x_r). \tag{1}$$

With the data already in CMP domain, a critical point is to choose the width of the CMP cells in the model, including a sufficient number of offsets to invert the parameters of each 1D model (see Figure 3), without overlaying many data of distinct receivers, avoiding instability and inversion artifacts.

For simplicity, the size of each CMP cell is regular and the model have the same length of receivers line.
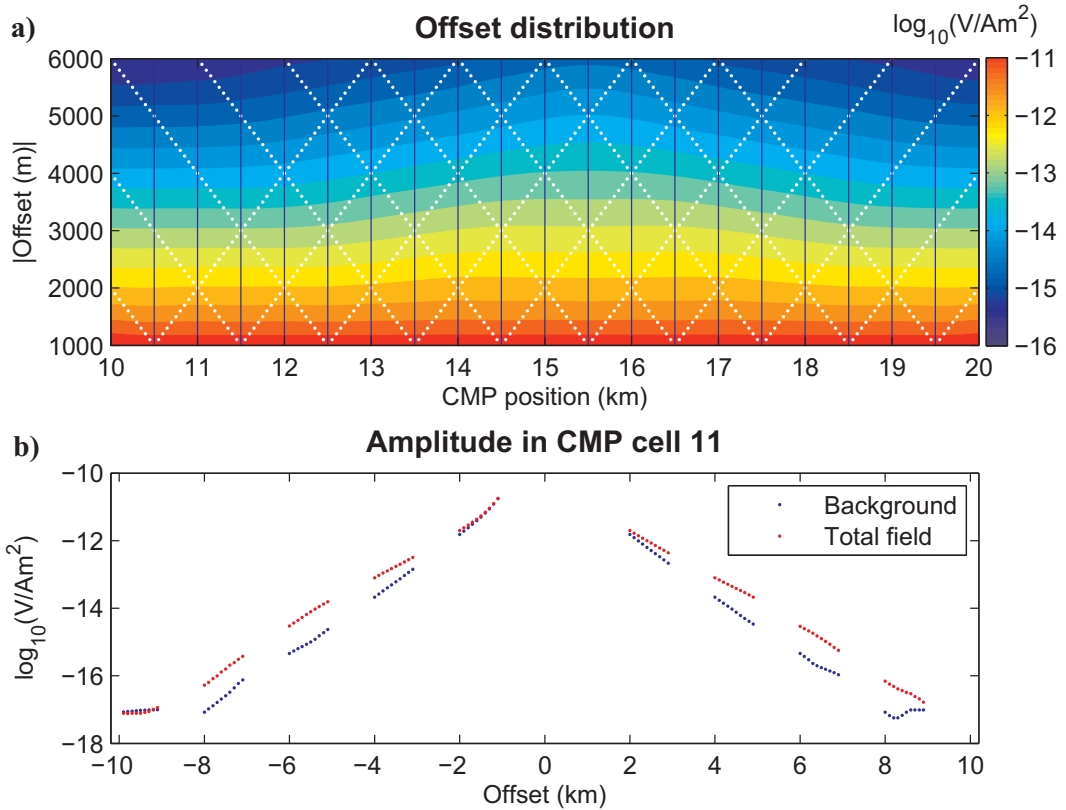
Figure 3

Figure 3: The (a) is the amplitude of total electric inline field at 0.75 Hz for the model of Figure 2, plotted as color map in coordinates of CMP position and offset modulus. Note that the resistive body increases the amplitude in central portion of the figure. Blue vertical lines 500-m apart, bound the CMP cells, white points shows the offsets distribution inside the CMP cells. The (b) presents the data of a CMP cell, at central region of the body, to clarify the gap in some offsets and the increase in amplitude due to the presence of the resistive body, in CMP domain.

Note in Figure 3, the CMP cells size of 500 m, as a half of the interval between receivers. That size allows a good offset distribution inside the cell, considering the overlap of both, the in-towing (negative offsets, as white dotted lines tilted to the left) and the out-towing (positive offsets, as white dotted lines tilted to the right). As for this 1D inversion, only the offsets modules are computed.

Figure 4 shows the increase in E-amplitude due to the presence of the 3D body, for a receiver close to the horizontal center of the body and for a CMP cell at the same region (red triangle and red lines in Figure 2). Note that CMP data is more sensitive to the body than receiver data for offsets longer than 3 km. The response for 1D body is also plotted, to show how the 3D body responses in CMP domain approximates to the response of 1D model.
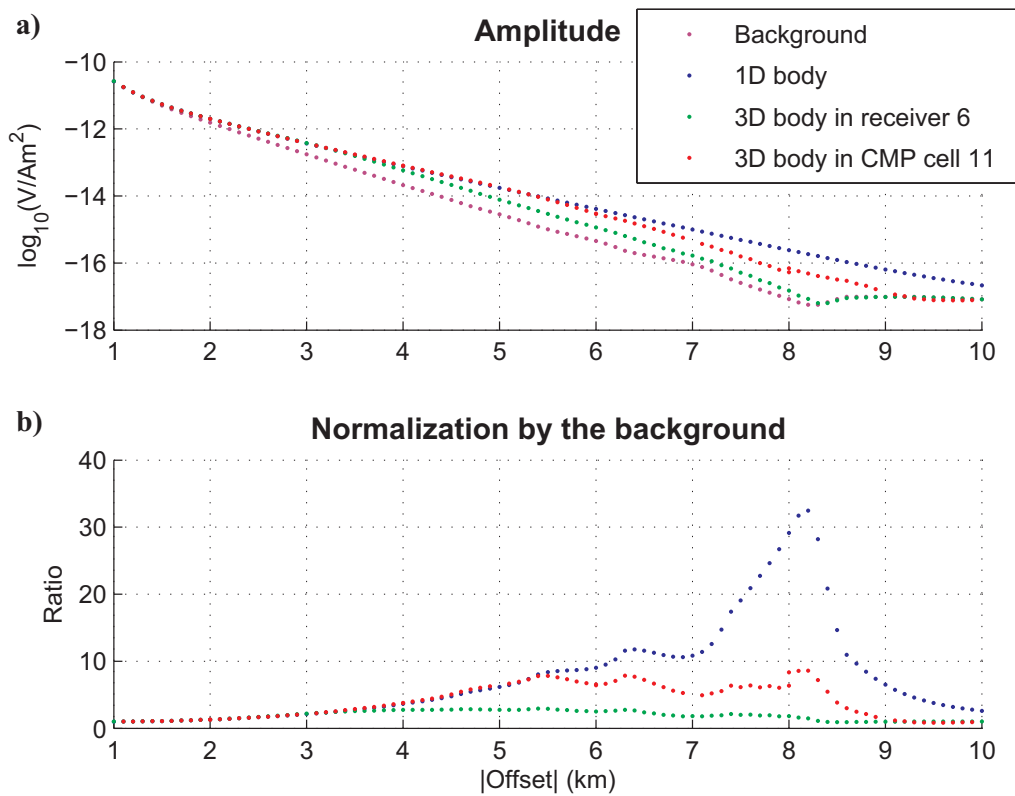
Figure 4

Figure 4: The (a) are the $|E_x|$ (0.75 Hz) curves for receiver-6 (green) and for CMP cell-11 (red), both in horizontal-central region of the 3D body. The blue dotted line is the response of a model in which the body was extended as a 1D layer with the same background, thickness, resistivity and depth of the 3D body. The (b) shows the normalization of the amplitude responses, for each situation in presence of bodies, by the background response. Note that until the offset 5.5 km, the effect of the 3D body in CMP domain is very close to 1D.

Inverse problem

The CMP inversion requires to laterally constrain the CMP cells (Auken et al., 2005) in order to address the effects of 2D and 3D structures, stabilizing the inversion and to introduce geological information.

Furthermore each CMP cell could be inverted for few layers, being stable to the data set, without regularization. However, as the resistivity transitions in sedimentary enviroments are usually smooth, there is more geological sense inverting a model with several layers with smoothed resistivity transitions, by the application of minimum vertical gradient operator (Constable et al., 1987); allowing some jumps in resistivity at interfaces mapped from seismic and resistivity well log. Also, it is possible to introduce a priori resistivity, constraining the inversion. Thus the objective function to be minimized is the L$_2$-norm of the residual, plus the three types of constraints (Tarantola, 2005), i.e.:

$$\phi = [(\mathbf{d} - \mathbf{F}(\mathbf{m}))^T \mathbf{W}_d (\mathbf{d} - \mathbf{F}(\mathbf{m})) + \chi^2] + [\mathbf{m}^T \nabla_h^T \mathbf{W}_h \nabla_h \mathbf{m}]$$
$$+ [\mathbf{m}^T \nabla_v^T \mathbf{W}_v \nabla_v \mathbf{m}] + [(\mathbf{m} - \mathbf{m}_p)^T \mathbf{W}_p (\mathbf{m} - \mathbf{m}_p)], \qquad (2)$$

where,
$\mathbf{d} = \{\log |E_x^{obs}(x_h, x_c, \omega)|\}$ is the vector of observed logarithmic amplitude of electric inline field, as a function of CMP cell, offset and angular frequency.
$\mathbf{F}(\mathbf{m}) = \{\log |E_x^{mod}(x_h, x_c, \omega)|\}$ is the vector of the responses for all 1D models, each corresponding to a CMP cell.

As the mCSEM data has strong amplitude decay along the offsets, the employment of the log-spaced amplitudes as data, naturally decreases the weight difference between near and far offsets, during the residual minimization, increasing sensitivity to deeper portions of the model.

$\mathbf{W}_d$ is a diagonal matrix, whose diagonal elements are set 1 as in present case the data error ϵ is not avaliable, however, in some cases it may be more efficient to raise some frequencies or offsets with respect to others.

$\chi^2 = \sum_{i=1}^{N} W_{ii}^d \epsilon_i^2$ is the total expected misfit of the data, in which subscript i is the data index of a vector with N elements. In the absence of data error values is set $\epsilon = 10^{-15}$.

$\mathbf{m} = \{\log(\rho_{l,c})\}$ is the parameter vector of logarithmic resistivities to be inverted, where the subscripts l and c refer to layer and CMP cell, respectively. The application of logarithm is to avoid negative resistivities.

∇_h is the first order discrete differential operator in horizontal direction (Auken and Christiansen, 2004).

∇_v is the first order discrete differential operator in vertical direction (Constable et al., 1987).

$\mathbf{W}_{\{h,v,p\}}$ is the weight diagonal matrix of constraints, whose elements related to free parameters should be equal to zero.

According to the theory of nonlinear inversion using the Marquardt algorithm (Marquardt, 1962), the estimated parameters must be searched through iterations, the kth iteration is:

$$\mathbf{m}_{k+1} = \mathbf{m}_k + \left[\mathbf{J}_k^T\mathbf{W}_d\mathbf{J}_k + \nabla_h^T\mathbf{W}_h\nabla_h + \nabla_v^T\mathbf{W}_v\nabla_v + \mathbf{W}_p + \mu\mathbf{I}\right]^{-1}$$
$$\cdot\left[(\mathbf{W}_d\mathbf{J}_k)^T(\mathbf{d} - \mathbf{F}(\mathbf{m}_k)) + \nabla_h^T\mathbf{W}_h\nabla_h\mathbf{m}_k + \nabla_v^T\mathbf{W}_v\nabla_v\mathbf{m}_k + \mathbf{W}_p(\mathbf{m}_k - \mathbf{m}_p)\right], \quad (3)$$

where, $\mathbf{J}$ is the Jacobian matrix, whose elements are calculated as:

$$J_{ij} = \frac{\partial\log|E_i|}{\partial\log(\rho_j)} = \frac{\rho_j}{|E_i|}\frac{\partial|E_i|}{\partial\rho_j} = \frac{\rho_j}{|E_i|^2}\mathfrak{Re}\left\{E_i^*\frac{\partial E_i}{\partial\rho_j}\right\}, \quad (4)$$

μ is the Marquardt parameter, $\mathbf{I}$ is the M-dimensional identity matrix, $\mathfrak{Re}$ means real part, and superscript $*$ denotes complex-conjugate.

Analytical derivatives

In order to reduce the inversion running time, were deduced the analytical derivatives of the fields with respect to the resistivities of the layers, needed to built the Jacobian matrix, Appendix B.

Figure 5 shows the running time comparison, between the simplest way to perform numerical derivatives (see Equation 5) and the analytical solution.

The finite difference algorithm used in the numerical derivative calculus for each layer is, for example:

$$\frac{\partial d_i(m_1, m_2, ..., m_M)}{\partial m_2} = \frac{d_i(m_1, m_2 + \Delta m_2, m_3, ..., m_M) - d_i(m_1, m_2 - \Delta m_2, m_3..., m_M)}{2\Delta m_2},$$
$$(5)$$

where, d_i is the ith of N data points generated by 1D HED forward function, and m_j is the jth of M resistivities to be inverted, remembering that the water layer is fixed.

Note that the forward function must be called $2 \cdot N \cdot M$ times for each iteration. Even with a very fast forward code, this process certainly is the one that takes more time in all inversion routines. On the other hand, a function that perform analytical derivatives for all

a)

Running time of derivatives

b)

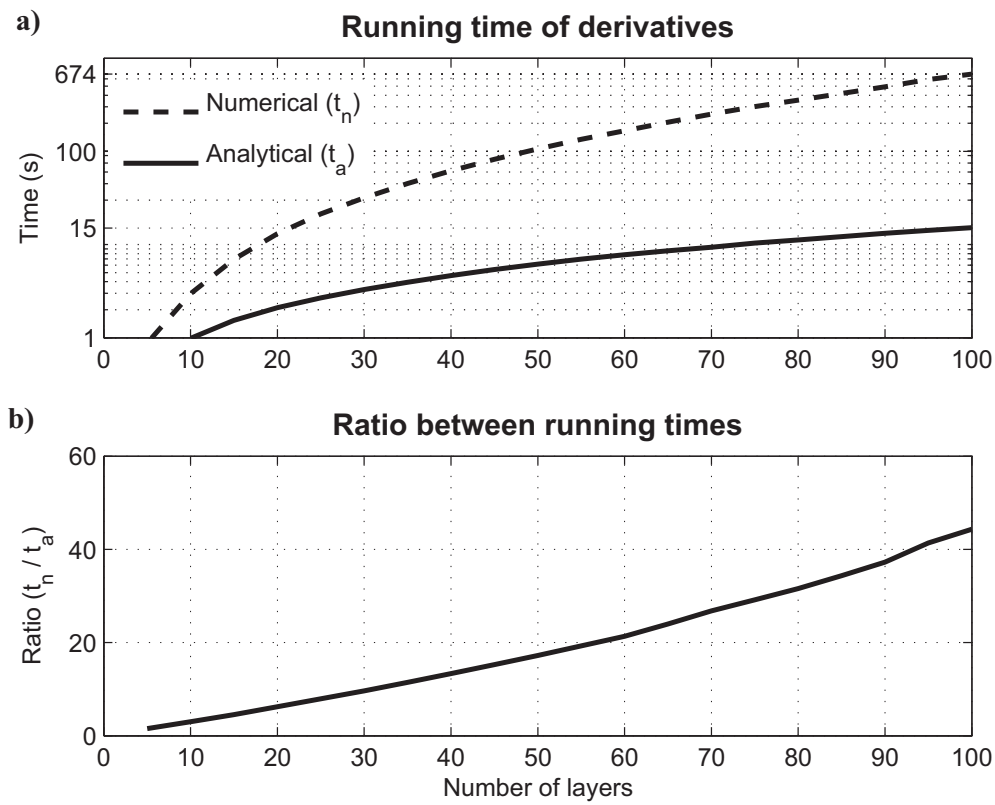**Ratio between running times**

Figure 5: The (a) are the running time of derivative calculus for 50 sources-receiver offsets, as a function of the number of layers, using an algorithm of finite differences (t_n as dashed line) and the analytical solution (t_a as solid line). The (b) is the ratio between the both curves in (a). Note the approximately linear increasing in the ratio plot.

M resistivities, must be called only N times. It explains approximated linear dependency in Figure 5(b).

It is recommended to assemble the forward and derivatives calculus in the same code, to use expressions and subroutines common to both, improving the computation.

SYNTHETIC DATA

Before applying the methodology to field data, it is important to perform some tests with synthetic data to evaluate the algorithms, to establish a work-flow and to tune the inversion. So the methodology was applied to the Ex response of the model in Figure 2, at 0.25 Hz, 0.75 Hz and 1.25 Hz, calculated by a 3D forward modeling based on Integral Equation (Zdhanov, 2009).

Starting model

As discussed before, regular horizontal discretization for the model is preferable. On the other hand, log-spaced layers are more consistent with the decrease in resolution along the depth, due to the diffusive nature of the fields.

The starting model was then built with fixed water layer and 150-Ωm-a priori resistivity for the bottom half-spaced layer to improve the inversion. All other cells have 1-Ωm-free resistivity, with vertical and horizontal smoothness, except the sea bottom and basement top transitions, whose vertical smoothness was removed, (see Figure 6).

Figure 6

The total relative percent error ($TRPE$) is given by:

$$TRPE = \frac{100}{N} \sum_{i=1}^{N} \left| \frac{|E_i^{mod}|}{|E_i^{obs}|} - 1 \right|. \tag{6}$$

Blind inversion

A preliminary blind inversion is performed without information about body position (see Figure 7), to assess the performance of the CMP technique of restoring the geometry of the original model. The only a priori information incorporated to this inversion is the depth and resistivity of the basement. The remaining part of the section to be inverted is regularized with vertical and horizontal smoothness, with diagonal elements of its respective weight matrix $W_h = 10$ and $W_v = 5$, applied over all free parameters.

Figure 7

The blind inversion of Figure 7 shows the ability of CMP inversion to recovering the central position of anomalous body as well as a sketch of background resitivities. The resistivity of the body is dramatically underestimated because of the smoothness operator as well as the 1D approach.
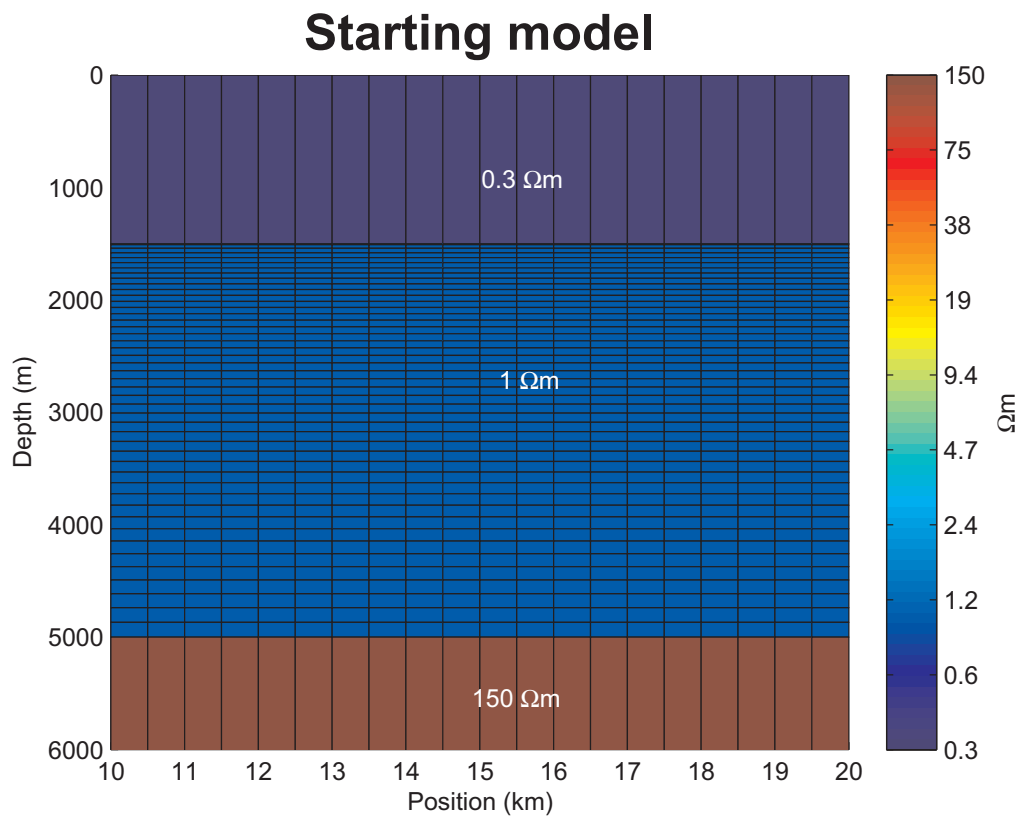
Figure 6: The residual $TRPE$ (see Equation 6), between synthetic and starting model, for $|E_x|$ at the three frequencies responses is 45.4 %. The water layers are not inverted, layers with 1 Ωm are free and the half-spaced bottom layer is constrained with 150-Ωm-a priori resistivity.
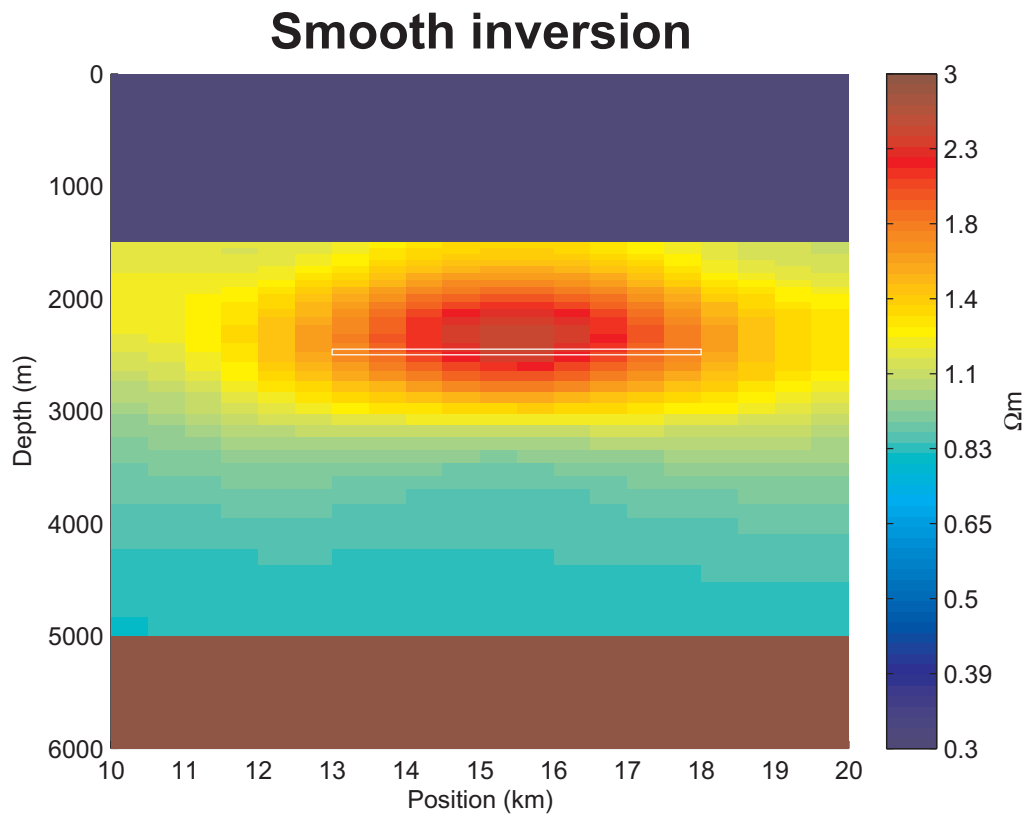
Figure 7: Inverted synthetic model with the horizontal and vertical smoothness operators applied over all section above 5 km. Note the recovered center of anomaly around the original body (in white lines). The $TRPE$ is 7.17 %, reached after 5 iterations.

Focused inversion

In order to recover a more accurate resistivity model, the smoothness at the body edges and at 2.5-km-depth background interface are removed (Key, 2009), (see Figure 8).
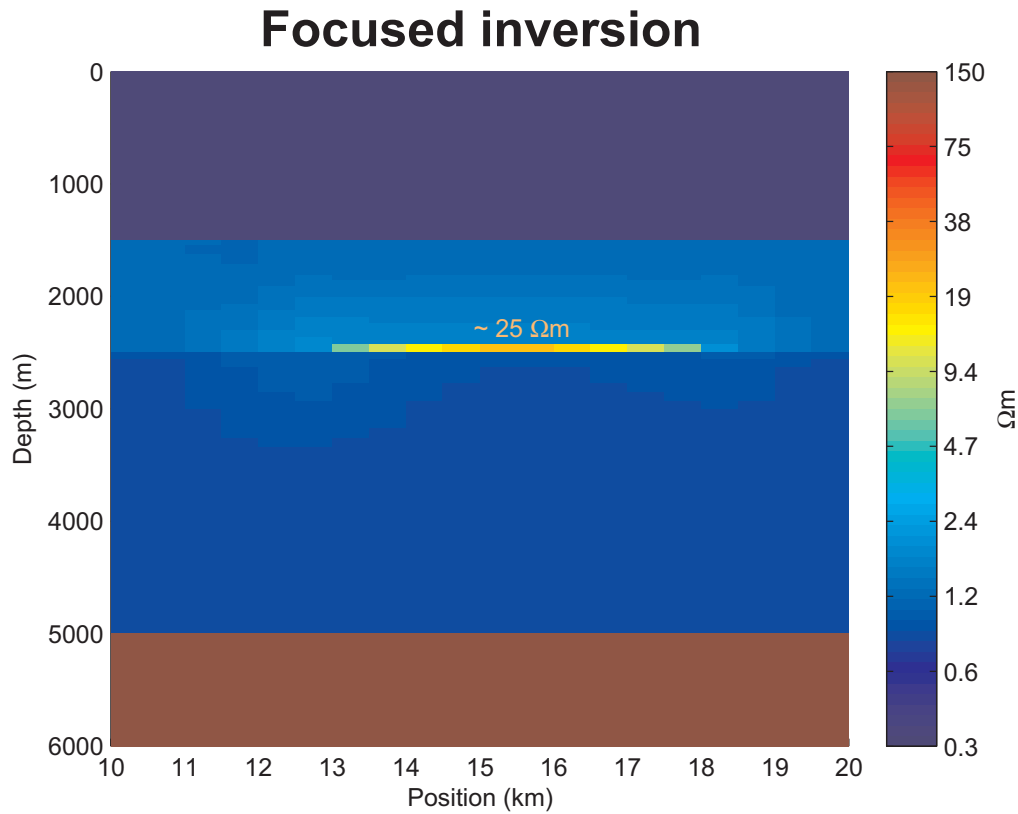
Figure 8

Focused inversion

Figure 8: In this focused inversion, the smoothness operators have the same weights of the blind inversion, except at the edges of the body and at 2.5-km-depth background interface, where smoothness weights are zero. The $TRPE$ is 6.8 %, reached after 15 iterations.

Figure 8 shows how the resistivities of the body cells approximates to the original as the cell is near to the center of the body, it means that, for central CMP cells, the effect of anomalous body is closer to a 1D layer effect, as expected.

In focused inversion, despite introducing information about the body position, the misfit is less than in the blind inversion, this is because the introduced information decreases the smoothness weight in objective function, enhancing the misfit minimization.

FIELD DATA

The mCSEM line LTAM10 was acquired in Santos Basin (Brasil)(see Figure 9), crossing a longitudinal lead with: 20 km of length and 5 km of width in the LTAM10 section. Oil has been found in a well in this reservoir at 2 km of distance from this line, where the well

log measures resistivities about 40 Ωm, along 50 m of a thick oil section (Buonora et al., 2008), (see Figure 10).
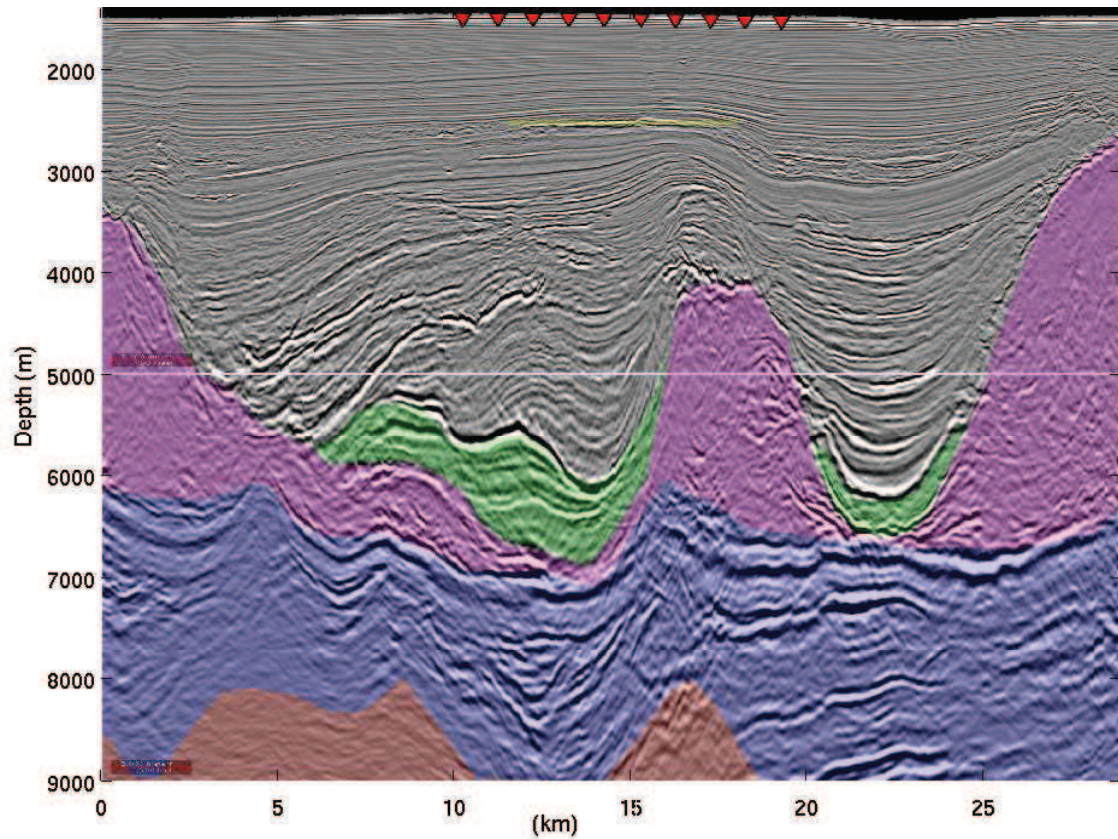
Figure 9

Figure 9: Seismic section along the LTAM10, red triangles at sea floor denotes receivers, the source positions are computed each 100 m along the line, and about 50 m above the bathimetry; the yellow rectangle indicates the region of the reservoir. Salt domes (magenta), carbonates (green), pré-salt (blue) and basement (red) lies on the deeper part of section.

Figure 10

To treat the bathimetry, each CMP cell have the first interface position as an average of the bathimetry inside the cell, and the z-position of the source is set 50 m above this interface for all 1D models. Apart from that, the simplicity of the stratigraphy above the lead and the high quality of the data allow the employment of a work-flow similar to the synthetic data, so the attention should be concentrated on the results.

Although deep, one should constraining with a priori resistivity, the salt domes and carbonates of the section in Figure 10, in order to improve the inversion (Key, 2009). So the starting model is shown in Figure 11.

Figure 11

For better visualizing the local misfit, instead of just calculating the $TRPE$, the relative percent error (RPE, see Equation 7) is plotted as function of CMP position and offset (see
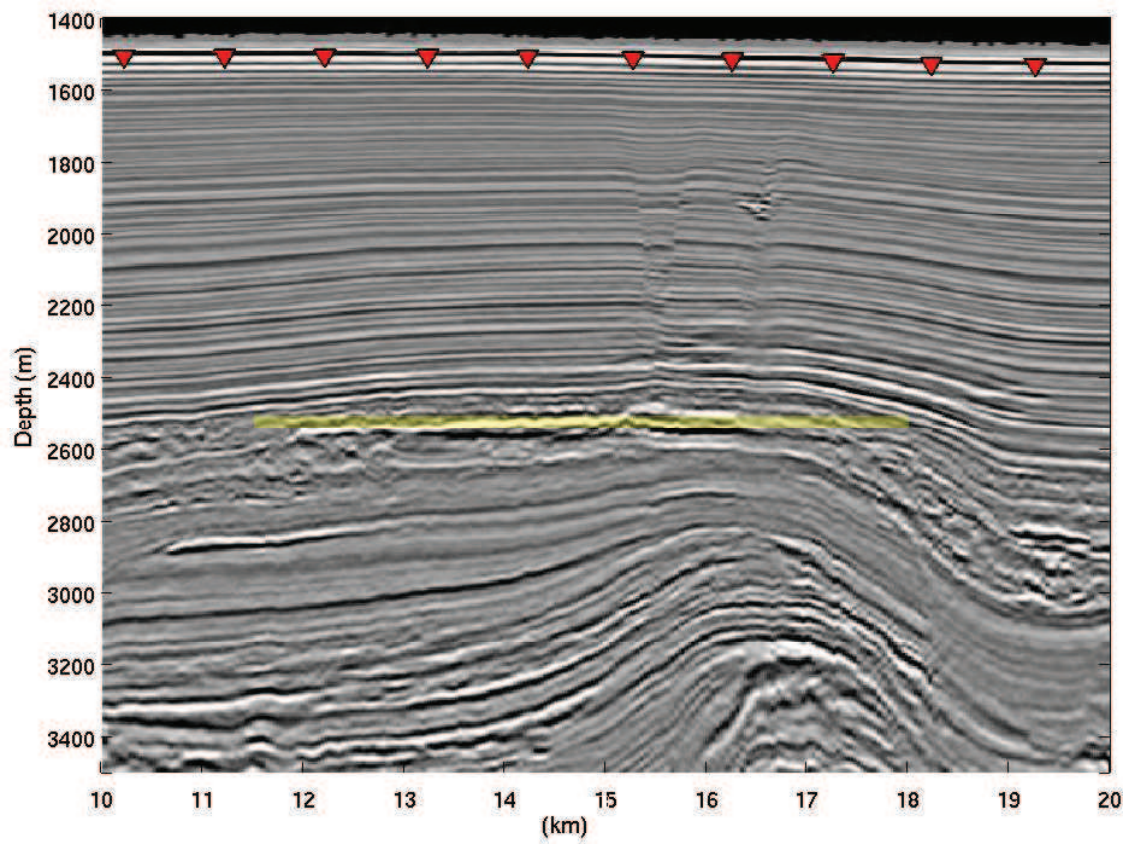
Figure 10: The target has 1 km of overburden, 50 m of thickness and is located between 12 km and 17 km along the line. The yellow rectangle represents the reservoir area whose edges have the smoothness removed, in focused inversion.
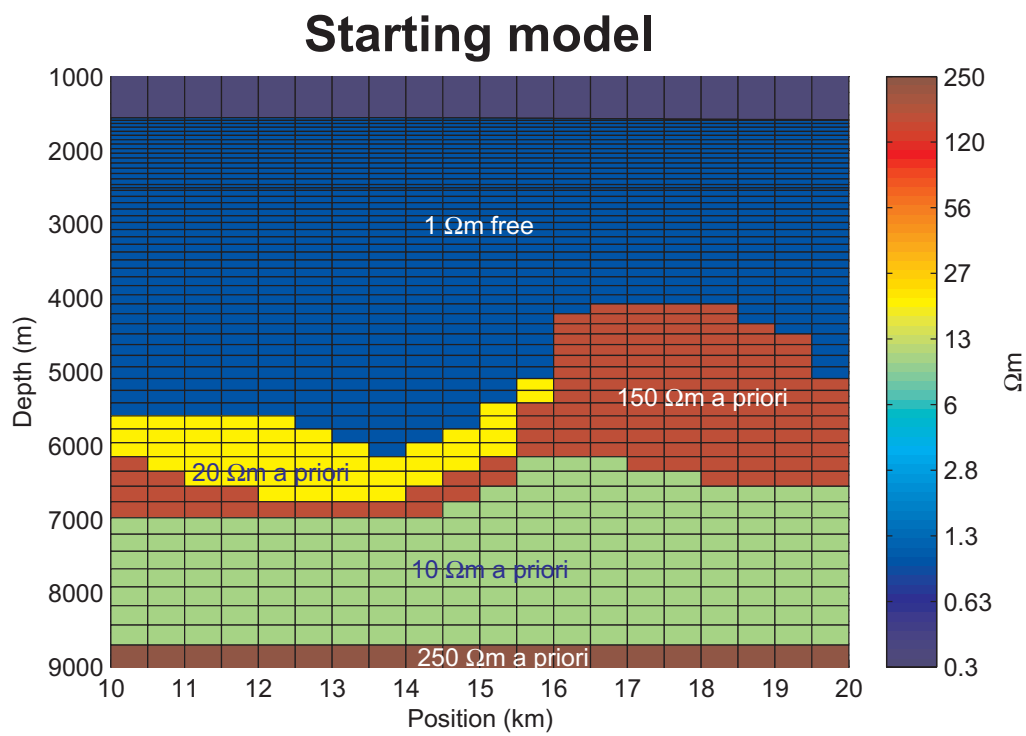
Starting model

Figure 11: In the starting model, the deeper structures are constrained with a priori, above at 2508-m-depth, another layer is added to the log-spaced layers, to delimit the top of the target. The $TRPE$ is 35.7 %.

Figure 12).

$$RPE = 100 \left| \frac{|E_i^{mod}|}{|E_i^{obs}|} - 1 \right|. \tag{7}$$

It is clear the high levels of RPE at the central portion of Figure 12, due to the resistive body effect, and in the far offsets, due to the noise level.
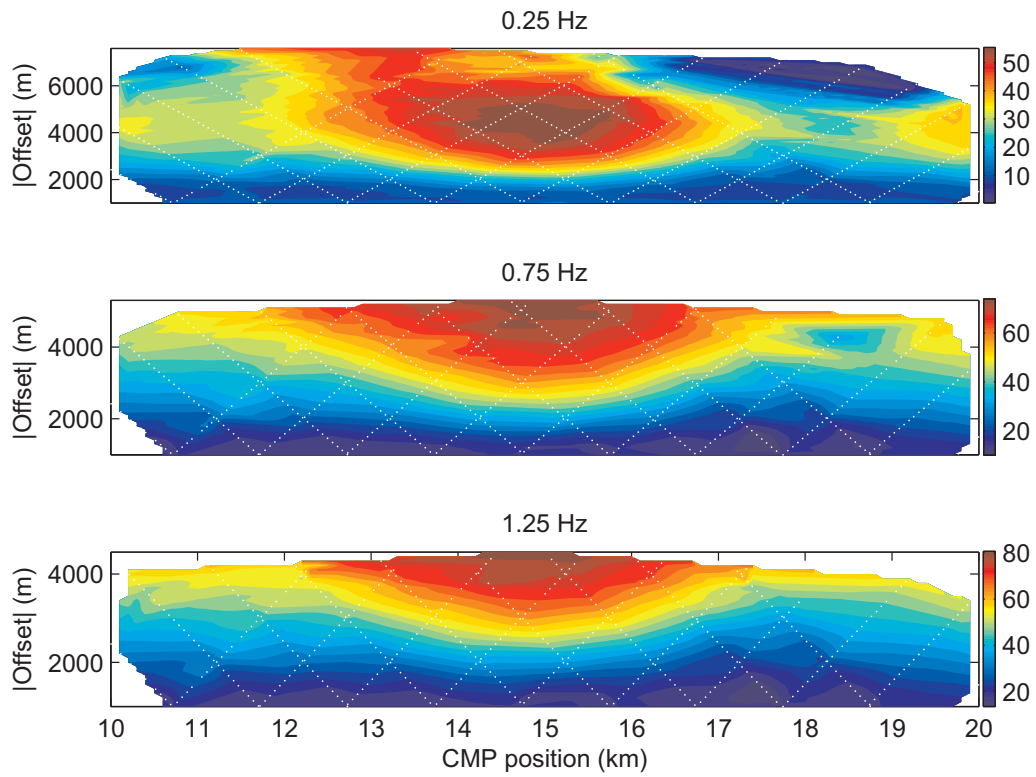
Figure 12

Figure 12: The RPE between the response of the starting model and the data is plotted for each frequency as function of CMP position and offset.

It is important to perform the blind inversion of Figure 13, before running the focused inversion, to asses three features: the data sensitivity to the body, the ability of the inversion to find the region of anomaly, in comparing with the seismics; and the presence of others anomalies in the section.

Figure 13

Figure 14 shows the decrease in misfit for all data. The bad misfit in central region of the 0.25-Hz-data is due to the body, as there is a jump of resistivity, the smoothness penalizes the data fitting.
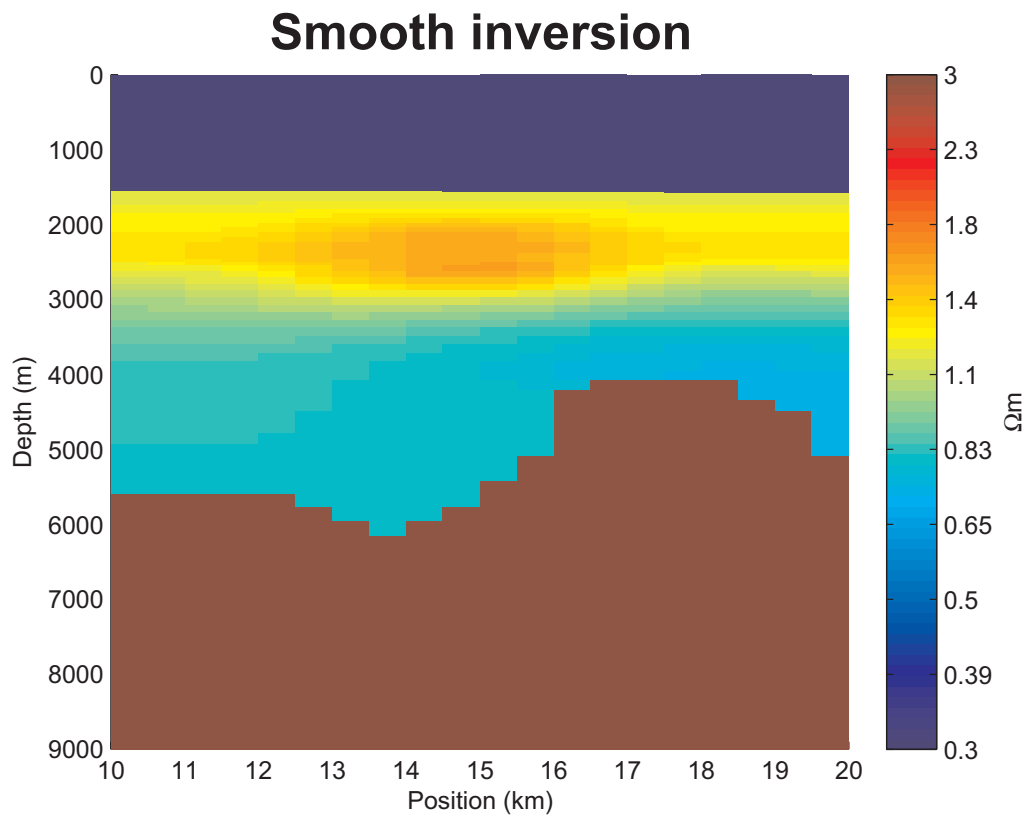
Figure 13: This blind inversion for LTAM10 data shows the sensibility of the data to the target, recovering its central position and it does not indicate the presence of another anomaly. This section is recovered with $TRPE = 7.58$ %, after 6 iterations.
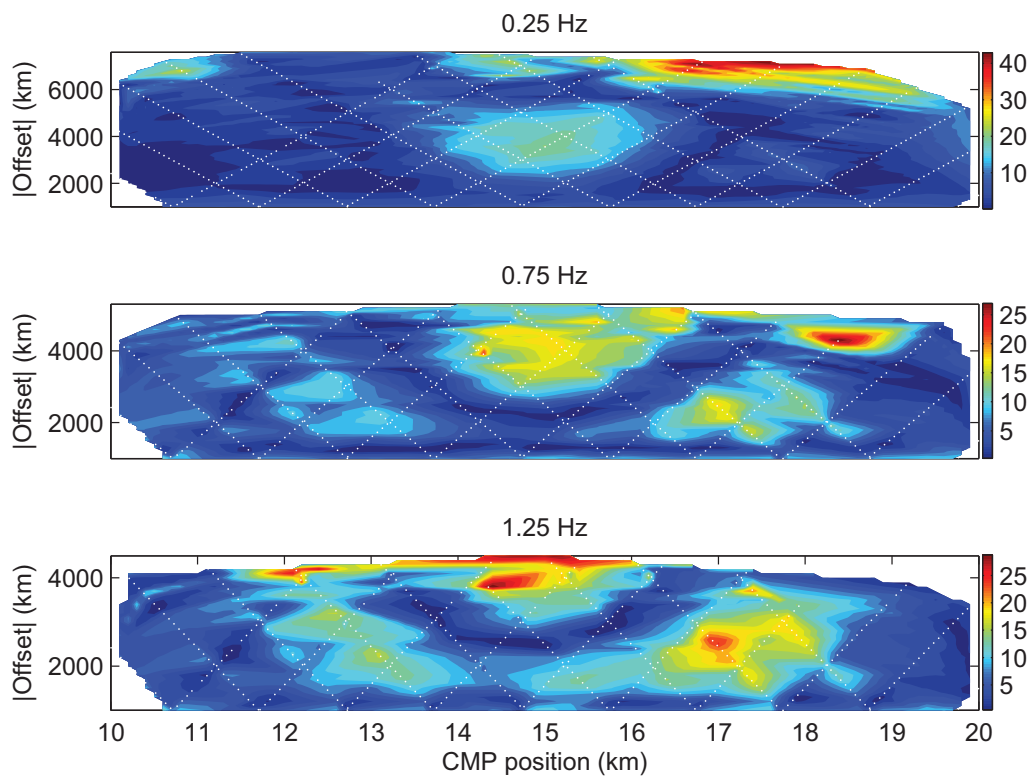
Figure 14: The residual RPE plot for blind inversion.

Figure 14

In performing the focused inversion of Figure 15, the smoothness is removed only in the body edges (the yellow rectangle in Figure 10), instead of remove this also in others seismic interfaces as in synthetic application, because it is not clear drops in resistivity, looking for the resistivity well log.
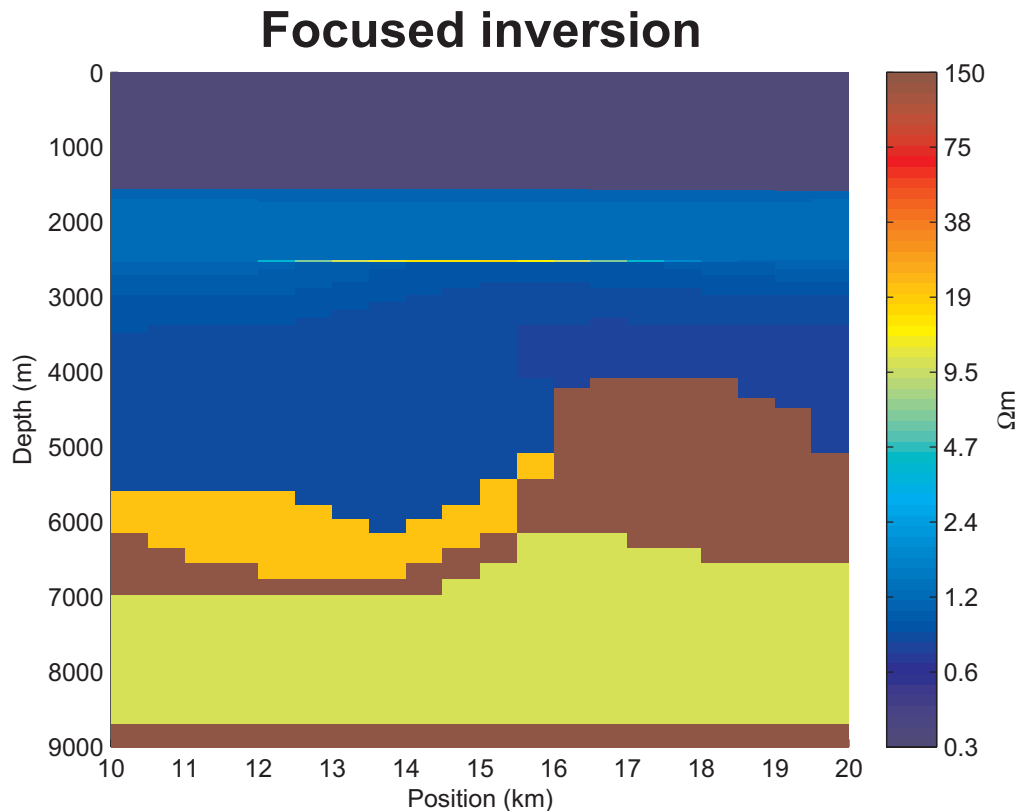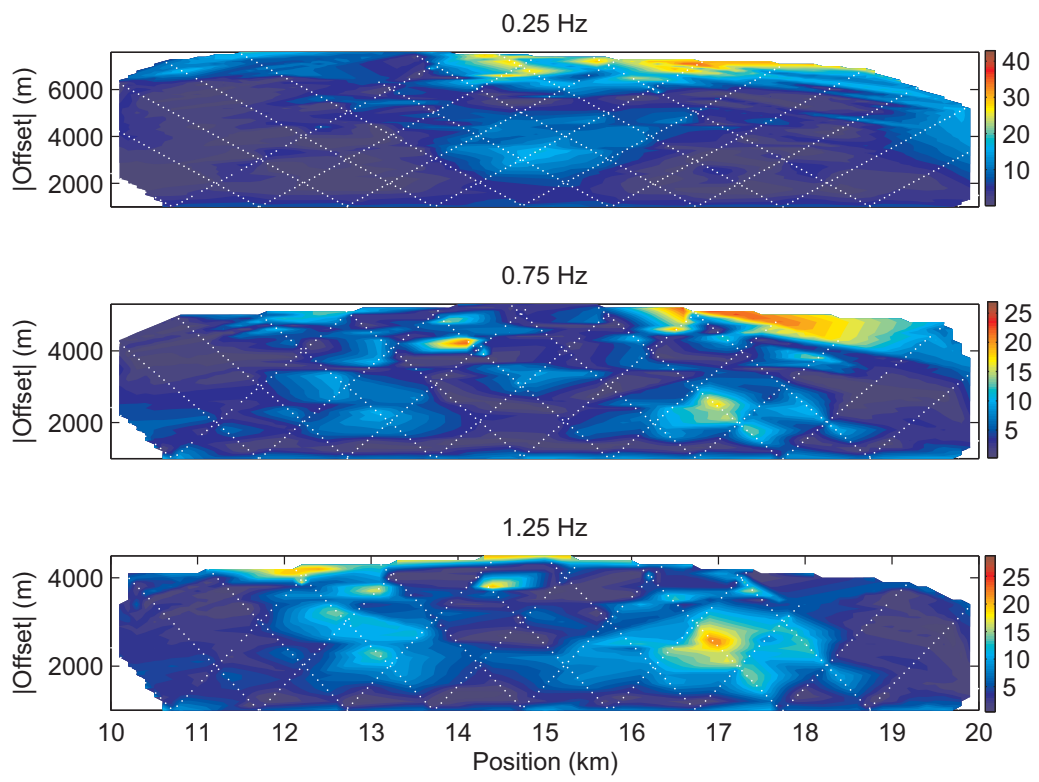
Figure 15

Figure 15: This focused inversion recovered about 20 Ωm in the center of the anomaly, with $TRPE = 6.27$ % after 11 interactions.

Figure 16 displays the misfit decrease of central portion, related to the removal of the smoothness around the body. It is curious the presence of bad misfit in the lateral edges of the body, probably due to edge effects, unexpected for 1D inversion, and limitations related to CMP methodology, which will be discussed in the next section.

Figure 16

Figure 17 shows the geoelectric section recovered co-rendered with seismic image, emphasizing the reservoir contrast and the background transition.

Figure 17

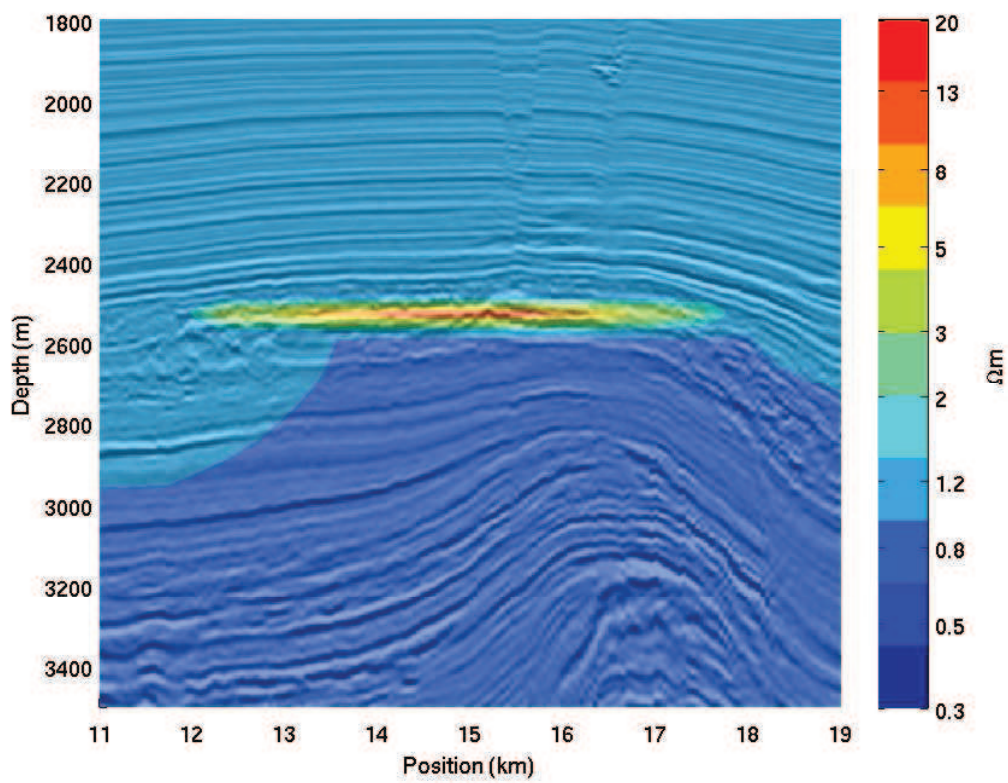Figure 16: The residual *RPE* plot for focused inversion.

Figure 17: This zoom in focused inversion superposed on seismic image, clearly shows the resistivity distribution recovered at the region of reservoir, and the transition of background resistivity.

DISCUSSIONS

An interpretative inputting of lateral constraints are essential to overcome the problem of nonlocal influence, inherent to the artifact of assigning a set of data to the parameters of only one CMP cell of the model to be inverted, because this set of data probably is under the influence of parameters of others CMP cells, generating inversion artifacts.

There are obviously others problems related to invert 3D structures with 1D inversion, as edge effects and deflections caused by lateral variations. Thus the most important limitation of this methodology is in the presence of strongly rough bathimetry. High anisotropy could also be a problem.

Models with few layers without vertical smoothness, according to seismic interpretation, were experimented, generating many inversion artifacts (Zdhanov, 2001), as well as, multilayered models with boundaries in smoothness over all seismic interpreted horizons have over-constrained the inversion (Hansen and Mittet, 1975).

CONCLUSION

The 1D CMP inversion with lateral constraints and interpretative boundaries has proved to be consistent in the synthetic application. Furthermore in field application, the higher resistivities in all cross-section above 5 km are recovered at the reservoir position, and some transitions in background resistivities are well correlated to the seismic interpretation and well log information.

The LTAM10 mCSEM profile is a friendly case history, mainly because of the quasi-layered sedimentation above the reservoir; however, this methodology has been successfully applied in more complex structures, by taking more interpretative application of the smoothness boundaries. Another particularity is that only the inline E_x amplitude was sufficient to invert the data, however in some cases as in broadside data, it could be useful to invert other components of E and H fields, as well as the phase, if this data has good signal to noise ratio.

The analytical derivatives has made it possible to recover this section in few minutes, even more, the analytical expressions clarify the dependencies and specific contributions to the electromagnetic problem.

Although underestimated, the recovered body resistivity contrast is about 20 times, confirming hydrocarbon in the reservoir. Summarizing, this kind of inversion in few minutes could be useful to exploratory works, because in natural sciences, the closer we can get to reality is an adequate visual representation.

ACKNOWLEDGMENTS

APPENDIX A

1D HED FIELDS

Following, are presented the solutions for electric and magnetic fields into the water (first layer) for our interesting case in which, receiver is under or at same depth of source and both in less or equal depth of the seafloor. These equations were deduced through Schelkunoff potentials and expressed in terms of Hankel transforms from Tocantins (2007).
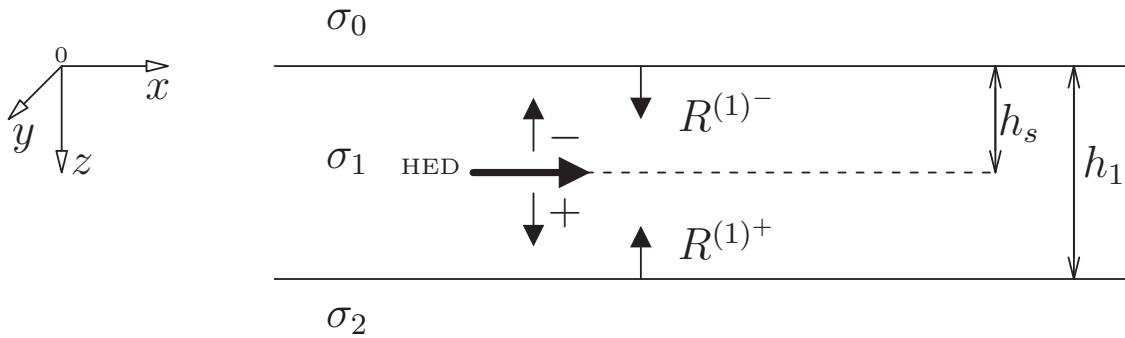
Figure A-1

Figure A-1: Horizontal electric dipole in the water layer and reflections coefficients above $R^{(1)-}$ and down $R^{(1)+}$ with respect to the dipole position.

$$
\begin{aligned}
E_x^{(1)} = &-\frac{Ids_x}{4\pi\delta^3}\rho_1\left(\frac{1}{\bar{r}}-\frac{2\bar{x}^2}{\bar{r}^3}\right)\int_0^\infty\left[e^{-\bar{u}_1(\bar{z}-\bar{h}_s)}+R_{TM}^{(1)-}e^{-\bar{u}_1(\bar{z}+\bar{h}_s)}+R_{TM}^{(1)+}e^{\bar{u}_1(\bar{z}+\bar{h}_s)}\right]\bar{u}_1 J_1(g\bar{r})dg \\
&-\frac{Ids_x}{4\pi\delta^3}\rho_1\frac{\bar{x}^2}{\bar{r}^2}\int_0^\infty\left[e^{-\bar{u}_1(\bar{z}-\bar{h}_s)}+R_{TM}^{(1)-}e^{-\bar{u}_1(\bar{z}+\bar{h}_s)}+R_{TM}^{(1)+}e^{\bar{u}_1(\bar{z}+\bar{h}_s)}\right]\bar{u}_1 g J_0(g\bar{r})dg \\
&-\frac{Ids_x}{4\pi\delta^3}\rho_1\left(\frac{1}{\bar{r}}-\frac{2\bar{y}^2}{\bar{r}^3}\right)\int_0^\infty\left[e^{-\bar{u}_1(\bar{z}-\bar{h}_s)}+R_{TE}^{(1)-}e^{-\bar{u}_1(\bar{z}+\bar{h}_s)}+R_{TE}^{(1)+}e^{\bar{u}_1(\bar{z}+\bar{h}_s)}\right]\frac{2i}{\bar{u}_1}J_1(g\bar{r})dg \\
&-\frac{Ids_x}{4\pi\delta^3}\rho_1\frac{\bar{y}^2}{\bar{r}^2}\int_0^\infty\left[e^{-\bar{u}_1(\bar{z}-\bar{h}_s)}+R_{TE}^{(1)-}e^{-\bar{u}_1(\bar{z}+\bar{h}_s)}+R_{TE}^{(1)+}e^{\bar{u}_1(\bar{z}+\bar{h}_s)}\right]\frac{2i}{\bar{u}_1}g J_0(g\bar{r})dg.
\end{aligned}
\tag{A-1}
$$

$$
\begin{aligned}
E_y^{(1)} = &+\frac{Ids_x}{4\pi\delta^3}\rho_1\frac{2\bar{x}\bar{y}}{\bar{r}^3}\int_0^\infty\left[e^{-\bar{u}_1(\bar{z}-\bar{h}_s)}+R_{TM}^{(1)-}e^{-\bar{u}_1(\bar{z}+\bar{h}_s)}+R_{TM}^{(1)+}e^{\bar{u}_1(\bar{z}+\bar{h}_s)}\right]\bar{u}_1 J_1(g\bar{r})dg \\
&-\frac{Ids_x}{4\pi\delta^3}\rho_1\frac{\bar{x}\bar{y}}{\bar{r}^2}\int_0^\infty\left[e^{-\bar{u}_1(\bar{z}-\bar{h}_s)}+R_{TM}^{(1)-}e^{-\bar{u}_1(\bar{z}+\bar{h}_s)}+R_{TM}^{(1)+}e^{\bar{u}_1(\bar{z}+\bar{h}_s)}\right]\bar{u}_1 g J_0(g\bar{r})dg \\
&-\frac{Ids_x}{4\pi\delta^3}\rho_1\frac{2\bar{x}\bar{y}}{\bar{r}^3}\int_0^\infty\left[e^{-\bar{u}_1(\bar{z}-\bar{h}_s)}+R_{TE}^{(1)-}e^{-\bar{u}_1(\bar{z}+\bar{h}_s)}+R_{TE}^{(1)+}e^{\bar{u}_1(\bar{z}+\bar{h}_s)}\right]\frac{2i}{\bar{u}_1}J_1(g\bar{r})dg \\
&+\frac{Ids_x}{4\pi\delta^3}\rho_1\frac{\bar{x}\bar{y}}{\bar{r}^2}\int_0^\infty\left[e^{-\bar{u}_1(\bar{z}-\bar{h}_s)}+R_{TE}^{(1)-}e^{-\bar{u}_1(\bar{z}+\bar{h}_s)}+R_{TE}^{(1)+}e^{\bar{u}_1(\bar{z}+\bar{h}_s)}\right]\frac{2i}{\bar{u}_1}g J_0(g\bar{r})dg.
\end{aligned}
\tag{A-2}
$$

$$
E_z^{(1)} = \frac{Ids_x}{4\pi\delta^3}\rho_1\frac{\bar{x}}{\bar{r}}\int_0^\infty\left[e^{-\bar{u}_1(\bar{z}-\bar{h}_s)}+R_{TM}^{(1)-}e^{-\bar{u}_1(\bar{z}+\bar{h}_s)}-R_{TM}^{(1)+}e^{\bar{u}_1(\bar{z}+\bar{h}_s)}\right]g^2 J_1(g\bar{r})dg.
\tag{A-3}
$$

$$H_x^{(1)} = - \frac{Ids_x}{4\pi\delta^2} \frac{2\bar{x}\bar{y}}{\bar{r}^3} \int_0^\infty \left[e^{-\bar{u}_1(\bar{z}-\bar{h}_s)} + R_{TM}^{(1)-} e^{-\bar{u}_1(\bar{z}+\bar{h}_s)} - R_{TM}^{(1)+} e^{\bar{u}_1(\bar{z}+\bar{h}_s)} \right] J_1(g\bar{r}) dg$$

$$+ \frac{Ids_x}{4\pi\delta^2} \frac{\bar{x}\bar{y}}{\bar{r}^2} \int_0^\infty \left[e^{-\bar{u}_1(\bar{z}-\bar{h}_s)} + R_{TM}^{(1)-} e^{-\bar{u}_1(\bar{z}+\bar{h}_s)} - R_{TM}^{(1)+} e^{\bar{u}_1(\bar{z}+\bar{h}_s)} \right] g J_0(g\bar{r}) dg$$

$$+ \frac{Ids_x}{4\pi\delta^2} \frac{2\bar{x}\bar{y}}{\bar{r}^3} \int_0^\infty \left[e^{-\bar{u}_1(\bar{z}-\bar{h}_s)} + R_{TE}^{(1)-} e^{-\bar{u}_1(\bar{z}+\bar{h}_s)} - R_{TE}^{(1)+} e^{\bar{u}_1(\bar{z}+\bar{h}_s)} \right] J_1(g\bar{r}) dg$$

$$- \frac{Ids_x}{4\pi\delta^2} \frac{\bar{x}\bar{y}}{\bar{r}^2} \int_0^\infty \left[e^{-\bar{u}_1(\bar{z}-\bar{h}_s)} + R_{TE}^{(1)-} e^{-\bar{u}_1(\bar{z}+\bar{h}_s)} - R_{TE}^{(1)+} e^{\bar{u}_1(\bar{z}+\bar{h}_s)} \right] g J_0(g\bar{r}) dg. \quad \text{(A-4)}$$

$$H_y^{(1)} = - \frac{Ids_x}{4\pi\delta^2} \left(\frac{1}{\bar{r}} - \frac{2\bar{x}^2}{\bar{r}^3} \right) \int_0^\infty \left[e^{-\bar{u}_1(\bar{z}-\bar{h}_s)} + R_{TM}^{(1)-} e^{-\bar{u}_1(\bar{z}+\bar{h}_s)} - R_{TM}^{(1)+} e^{\bar{u}_1(\bar{z}+\bar{h}_s)} \right] J_1(g\bar{r}) g$$

$$- \frac{Ids_x}{4\pi\delta^2} \frac{\bar{x}^2}{\bar{r}^2} \int_0^\infty \left[e^{-\bar{u}_1(\bar{z}-\bar{h}_s)} + R_{TM}^{(1)-} e^{-\bar{u}_1(\bar{z}+\bar{h}_s)} - R_{TM}^{(1)+} e^{\bar{u}_1(\bar{z}+\bar{h}_s)} \right] g J_0(g\bar{r}) dg$$

$$- \frac{Ids_x}{4\pi\delta^2} \left(\frac{1}{\bar{r}} - \frac{2\bar{y}^2}{\bar{r}^3} \right) \int_0^\infty \left[e^{-\bar{u}_1(\bar{z}-\bar{h}_s)} + R_{TE}^{(1)-} e^{-\bar{u}_1(\bar{z}+\bar{h}_s)} - R_{TE}^{(1)+} e^{\bar{u}_1(\bar{z}+\bar{h}_s)} \right] J_1(g\bar{r}) dg$$

$$- \frac{Ids_x}{4\pi\delta^2} \frac{\bar{y}^2}{\bar{r}^2} \int_0^\infty \left[e^{-\bar{u}_1(\bar{z}-\bar{h}_s)} + R_{TE}^{(1)-} e^{-\bar{u}_1(\bar{z}+\bar{h}_s)} - R_{TE}^{(1)+} e^{\bar{u}_1(\bar{z}+\bar{h}_s)} \right] g J_0(g\bar{r}) dg. \quad \text{(A-5)}$$

$$H_z^{(1)} = \frac{Ids_x}{4\pi\delta^2} \frac{\bar{y}}{\bar{r}} \int_0^\infty \left[e^{-\bar{u}_1(\bar{z}-\bar{h}_s)} + R_{TE}^{(1)-} e^{-\bar{u}_1(\bar{z}+\bar{h}_s)} + R_{TE}^{(1)+} e^{\bar{u}_1(\bar{z}+\bar{h}_s)} \right] \frac{g^2}{\bar{u}_1} J_1(g\bar{r}) dg. \quad \text{(A-6)}$$

Where $R^{(1)-}$ are downward and $R^{(1)+}$ upward reflections coefficients in both TM and TE modes.

TE mode

$$R_{TE}^{(1)-} = \frac{\dfrac{\bar{u}_1 - \bar{u}_0}{\bar{u}_1 + \bar{u}_0} \left(1 + \dfrac{\bar{u}_1 - F_2^{TE}\bar{u}_2}{\bar{u}_1 + F_2^{TE}\bar{u}_2} e^{-2\bar{u}_1(\bar{h}_1-\bar{h}_s)} \right)}{1 - \dfrac{\bar{u}_1 - \bar{u}_0}{\bar{u}_1 + \bar{u}_0} \left(\dfrac{\bar{u}_1 - F_2^{TE}\bar{u}_2}{\bar{u}_1 + F_2^{TE}\bar{u}_2} \right) e^{-2\bar{u}_1\bar{h}_1}}, \quad \text{(A-7)}$$

$$R_{TE}^{(1)+} = \frac{\dfrac{\bar{u}_1 - F_2^{TE}\bar{u}_2}{\bar{u}_1 + F_2^{TE}\bar{u}_2} \left(1 + \dfrac{\bar{u}_1 - \bar{u}_0}{\bar{u}_1 + \bar{u}_0} e^{-2\bar{u}_1\bar{h}_s} \right) e^{-2\bar{u}_1\bar{h}_1}}{1 - \dfrac{\bar{u}_1 - \bar{u}_0}{\bar{u}_1 + \bar{u}_0} \left(\dfrac{\bar{u}_1 - F_2^{TE}\bar{u}_2}{\bar{u}_1 + F_2^{TE}\bar{u}_2} \right) e^{-2\bar{u}_1\bar{h}_1}}, \quad \text{(A-8)}$$

with TE stratification factor as

$$F_j^{TE} = \frac{\bar{u}_{j+1} F_{j+1}^{TE} + \bar{u}_j \tanh[\bar{u}_j\bar{h}_j]}{\bar{u}_j + \bar{u}_{j+1} F_{j+1}^{TE} \tanh[\bar{u}_j\bar{h}_j]}, \qquad j = 2, ..., N-1 \quad \text{(A-9)}$$

$$F_N^{TE} = 1.$$

The same for TM mode

$$R_{TM}^{(1)-} = \frac{1 - \dfrac{\rho_1 \bar{u}_1 - \rho_2 F_2^{TM} \bar{u}_2}{\rho_1 \bar{u}_1 + \rho_2 F_2^{TM} \bar{u}_2} e^{-2\bar{u}_1(\bar{h}_1 - \bar{h}_s)}}{1 + \left(\dfrac{\rho_1 \bar{u}_1 - \rho_2 F_2^{TM} \bar{u}_2}{\rho_1 \bar{u}_1 + \rho_2 F_2^{TM} \bar{u}_2}\right) e^{-2\bar{u}_1 \bar{h}_1}}, \tag{A-10}$$

$$R_{TM}^{(1)+} = \frac{-\dfrac{\rho_1 \bar{u}_1 - \rho_2 F_2^{TM} \bar{u}_2}{\rho_1 \bar{u}_1 + \rho_2 F_2^{TM} \bar{u}_2} \left(1 + e^{-2u_1 h_s}\right) e^{-2\bar{u}_1 \bar{h}_1}}{1 + \left(\dfrac{\rho_1 \bar{u}_1 - \rho_2 F_2^{TM} \bar{u}_2}{\rho_1 \bar{u}_1 + \rho_2 F_2^{TM} \bar{u}_2}\right) e^{-2\bar{u}_1 \bar{h}_1}}, \tag{A-11}$$

with

$$F_j^{TM} = \frac{\rho_{j+1} \bar{u}_{j+1} F_{j+1}^{TM} + \rho_j \bar{u}_j \tanh[\bar{u}_j \bar{h}_j]}{\rho_j \bar{u}_j + \rho_{j+1} \bar{u}_{j+1} F_{j+1}^{TM} \tanh[\bar{u}_j \bar{h}_j]}, \qquad j = 2, ..., N-1 \tag{A-12}$$

$$F_N^{TM} = 1.$$

Where,

J_0 and J_1 are Bessel functions of first kind of zero and first order respectively.

δ is the water skin-depth. All quantities under a bar are normalized by δ .

j index refers to the layer, thus $j = 0$ is the air, $j = 1$ is the water, $j = N$ is the half-space layer.

ρ and $\bar{h}$ are resistivities and thicknesses of layers respectively.

$\bar{h}_s$ is the depth of the source.

$\bar{z}$ is the depth of the receiver.

$\bar{u}_j = \sqrt{g^2 + 2i\dfrac{\rho_1}{\rho_j}}$ is the diffusion term in wick $i = \sqrt{-1}$ and g is the integration term, note that $\bar{u}_0 = g$ since the resistivity of the air go to infinite.

Ids_x is the dipole moment.

An important point of this formulation is that all quantities involved are normalized by the water skin-depth, in order to improve the computation.

APPENDIX B

DERIVATIVES

In order to calculate derivatives of the fields, one should just substitute derivatives of the reflection coefficients with respect to the resistivity of the layers in place where there is these coefficients in the integrals and turn to zero the first term of the sum.

Total derivative of the reflection coefficients could be formulated as:

$$\frac{dR^{(1)}}{d\rho_j} = \frac{\partial R^{(1)}}{\partial \rho_j} + \frac{\partial R^{(1)}}{\partial F_2} \frac{\partial F_2}{\partial \rho_j}. \tag{B-1}$$

Special cases: if $j = 2 = N$ the second term turn in to zero, if $j = 2 < N$ there are both terms. In here is presented partial derivatives for these special cases:

$$\frac{\partial R_{TE}^{(1)-}}{\partial \rho_2} = \frac{-2\bar{u}_1 \bar{u}_2' F_2^{TE} \left(e^{2\bar{u}_1 \bar{h}_s} + \frac{\bar{u}_1 - \bar{u}_0}{\bar{u}_1 + \bar{u}_0} \right) \frac{\bar{u}_1 - \bar{u}_0}{\bar{u}_1 + \bar{u}_0} e^{-2\bar{u}_1 \bar{h}_1}}{\left[\bar{u}_1 + \bar{u}_2 F_2^{TE} - \frac{\bar{u}_1 - \bar{u}_0}{\bar{u}_1 + \bar{u}_0} \left(\bar{u}_1 - \bar{u}_2 F_2^{TE} \right) e^{-2\bar{u}_1 \bar{h}_1} \right]^2}, \tag{B-2}$$

$$\frac{\partial R_{TE}^{(1)-}}{\partial F_2^{TE}} = \frac{-2\bar{u}_1 \bar{u}_2 \left(e^{2\bar{u}_1 \bar{h}_s} + \frac{\bar{u}_1 - \bar{u}_0}{\bar{u}_1 + \bar{u}_0} \right) \frac{\bar{u}_1 - \bar{u}_0}{\bar{u}_1 + \bar{u}_0} e^{-2\bar{u}_1 \bar{h}_1}}{\left[\bar{u}_1 + \bar{u}_2 F_2^{TE} - \frac{\bar{u}_1 - \bar{u}_0}{\bar{u}_1 + \bar{u}_0} \left(\bar{u}_1 - \bar{u}_2 F_2^{TE} \right) e^{-2\bar{u}_1 \bar{h}_1} \right]^2}, \tag{B-3}$$

$$\frac{\partial R_{TE}^{(1)+}}{\partial \rho_2} = \frac{-2\bar{u}_1 \bar{u}_2' F_2^{TE} R_{TE}^{(1)+}}{\bar{u}_1^2 - \left(\bar{u}_2 F_2^{TE} \right)^2 - \frac{\bar{u}_1 - \bar{u}_0}{\bar{u}_1 + \bar{u}_0} \left(\bar{u}_1 - \bar{u}_2 F_2^{TE} \right)^2 e^{-2\bar{u}_1 \bar{h}_1}}, \tag{B-4}$$

$$\frac{\partial R_{TE}^{(1)+}}{\partial F_2^{TE}} = \frac{-2\bar{u}_1 \bar{u}_2 R_{TE}^{(1)+}}{\bar{u}_1^2 - \left(\bar{u}_2 F_2^{TE} \right)^2 - \frac{\bar{u}_1 - \bar{u}_0}{\bar{u}_1 + \bar{u}_0} \left(\bar{u}_1 - \bar{u}_2 F_2^{TE} \right)^2 e^{-2\bar{u}_1 \bar{h}_1}}, \tag{B-5}$$

$$\frac{\partial R_{TM}^{(1)-}}{\partial \rho_2} = \frac{2\rho_1 \bar{u}_1 F_2^{TM} \left(\bar{u}_2 + \rho_2 \bar{u}_2' \right) \left(1 + e^{2\bar{u}_1 \bar{h}_s} \right) e^{-2\bar{u}_1 \bar{h}_1}}{\left[\rho_1 \bar{u}_1 + \rho_2 \bar{u}_2 F_2^{TM} + \left(\rho_1 \bar{u}_1 - \rho_2 \bar{u}_2 F_2^{TM} \right) e^{-2\bar{u}_1 \bar{h}_1} \right]^2}, \tag{B-6}$$

$$\frac{\partial R_{TM}^{(1)-}}{\partial F_2^{TM}} = \frac{2\rho_1 \bar{u}_1 \rho_2 \bar{u}_2 \left(1 + e^{2\bar{u}_1 \bar{h}_s} \right) e^{-2\bar{u}_1 \bar{h}_1}}{\left[\rho_1 \bar{u}_1 + \rho_2 \bar{u}_2 F_2^{TM} + \left(\rho_1 \bar{u}_1 - \rho_2 \bar{u}_2 F_2^{TM} \right) e^{-2\bar{u}_1 \bar{h}_1} \right]^2}, \tag{B-7}$$

$$\frac{\partial R_{TM}^{(1)+}}{\partial \rho_2} = \frac{2\rho_1 \bar{u}_1 F_2^{TM} \left(\bar{u}_2 + \rho_2 \bar{u}_2' \right) \left(1 + e^{-2\bar{u}_1 \bar{h}_s} \right) e^{-2\bar{u}_1 \bar{h}_1}}{\left[\rho_1 \bar{u}_1 + \rho_2 \bar{u}_2 F_2^{TM} + \left(\rho_1 \bar{u}_1 - \rho_2 \bar{u}_2 F_2^{TM} \right) e^{-2\bar{u}_1 \bar{h}_1} \right]^2}, \tag{B-8}$$

$$\frac{\partial R_{TM}^{(1)+}}{\partial F_2^{TM}} = \frac{2\rho_1 \bar{u}_1 \rho_2 \bar{u}_2 \left(1 + e^{-2\bar{u}_1 \bar{h}_s} \right) e^{-2\bar{u}_1 \bar{h}_1}}{\left[\rho_1 \bar{u}_1 + \rho_2 \bar{u}_2 F_2^{TM} + \left(\rho_1 \bar{u}_1 - \rho_2 \bar{u}_2 F_2^{TM} \right) e^{-2\bar{u}_1 \bar{h}_1} \right]^2}. \tag{B-9}$$

For $N \geq j > 2$, the chain rule leads to

$$\frac{dR^{(1)}}{d\rho_j} = \frac{\partial R^{(1)}}{\partial F_2} \left(\prod_{i=2}^{j-2} \frac{\partial F_i}{\partial F_{i+1}} \right) \left(\frac{\partial F_{j-1}}{\partial \rho_j} + \frac{\partial F_{j-1}}{\partial F_j} \frac{\partial F_j}{\partial \rho_j} \right). \tag{B-10}$$

If $j = 3 \leq N$ the first term in parenthesis is equal 1. Note that if $j = N$, the second term in the sum is null.

Now, the partial derivatives of stratification factors are.

$$\frac{\partial F_j^{TE}}{\partial F_{j+1}^{TE}} = \frac{\bar{u}_j \bar{u}_{j+1} \text{sech}^2[\bar{u}_j \bar{h}_j]}{\left(\bar{u}_j + \bar{u}_{j+1} F_{j+1}^{TE} \tanh[\bar{u}_j \bar{h}_j] \right)^2}, \tag{B-11}$$

$$\frac{\partial F_j^{TE}}{\partial \rho_j} = \frac{\bar{u}_j' \left[\bar{u}_j^2 \bar{h}_j - \bar{u}_{j+1} F_{j+1}^{TE} \left(1 + \bar{u}_{j+1} F_{j+1}^{TE} \bar{h}_j \right) \right] \text{sech}^2[\bar{u}_j \bar{h}_j]}{\left(\bar{u}_j + \bar{u}_{j+1} F_{j+1}^{TE} \tanh[\bar{u}_j \bar{h}_j] \right)^2}, \tag{B-12}$$

$$\frac{\partial F_j^{TE}}{\partial \rho_{j+1}} = \frac{\bar{u}_{j+1}' F_{j+1}^{TE} \left(1 - F_j^{TE} \tanh[\bar{u}_j \bar{h}_j] \right)}{\bar{u}_j + \bar{u}_{j+1} F_{j+1}^{TE} \tanh[\bar{u}_j \bar{h}_j]}, \tag{B-13}$$

$$\frac{\partial F_j^{TM}}{\partial F_{j+1}^{TM}} = \frac{\rho_j \bar{u}_j \rho_{j+1} \bar{u}_{j+1} \text{sech}^2[\bar{u}_j \bar{h}_j]}{\left(\rho_j \bar{u}_j + \rho_{j+1} \bar{u}_{j+1} F_{j+1}^{TM} \tanh[\bar{u}_j \bar{h}_j] \right)^2}, \tag{B-14}$$

$$\frac{\partial F_j^{TM}}{\partial \rho_j} = \frac{\left[\rho_j^2 \bar{u}_j^2 \bar{u}_j' \bar{h}_j - \rho_{j+1} \bar{u}_{j+1} F_{j+1}^{TM} \left(\bar{u}_j + \rho_j \bar{u}_j' + \bar{u}_j' \bar{h}_j \rho_{j+1} \bar{u}_{j+1} F_{j+1}^{TM} \right) \right] \text{sech}^2[\bar{u}_j \bar{h}_j]}{\left(\rho_j \bar{u}_j + \rho_{j+1} \bar{u}_{j+1} F_{j+1}^{TM} \tanh[\bar{u}_j \bar{h}_j] \right)^2}, \tag{B-15}$$

$$\frac{\partial F_j^{TM}}{\partial \rho_{j+1}} = \frac{F_{j+1}^{TM} \left(\bar{u}_{j+1} + \rho_{j+1} \bar{u}_{j+1}' \right) \left(1 - F_j^{TM} \tanh[\bar{u}_j \bar{h}_j] \right)}{\rho_j \bar{u}_j + \rho_{j+1} \bar{u}_{j+1} F_{j+1}^{TM} \tanh[\bar{u}_j \bar{h}_j]}. \tag{B-16}$$

Where $\bar{u}_j' = \frac{\partial \bar{u}_j}{\partial \rho_j} = \frac{-i \rho_1}{\rho_j^2 \bar{u}_j}$.

It is recommended to substitute the term $e^{-2\bar{u}_1 \bar{h}_1}$ in calculus of $R^{(1)+}$ directly inside the integrals, to prevent numerical divergences.

REFERENCES

Auken, E., and A. V. Christiansen, 2004, Layered and laterally constrained 2d inversion of resistivity data: Geophysics, **69**, 752–761.

Auken, E., A. V. Christiansen, B. H. Jacobsen, N. Foged, and K. I. Sørensen, 2005, Piecewise 1d laterally costraine inversion of resistivity data: Geophysical Prospecting, **53**, 497–506.

Buonora, M. P., A. Zerilli, and T. Lambruzzo, 2008, Advancing marine controlled source electromagnetics in the santos basin, brazi: 70th EAGE Conference and Exhibition incorporating SPE EUROPEC 2008, Europ. Assoc. of Geosc. and Eng., Session:G008.

Christensen, N., and K. Dodds, 2007, Marine controlled-source electromagnetic methods 1d inversion and resolution analysis of marine csem data: Geophysics, **72**, WA27–WA38.

Constable, S. C., R. L. Parker, and C. G. Constable, 1987, Occam' inversion: A practical algorithm for generatlng smooth models from electromagnetic sounding data: Geophysics, **52**, 289–300.

Constable, S. C., and C. J. Weiss, 2006, Mapping thin resistors and hydrocarbons with marine em methods: Insights from 1d madeling: Geophysics, **71**, G43–G51.

Eidesmo, T., S. Ellingsrud, L. M. MacGregor, S. Constable, M. C. Sinha, S. J. F. N. Kong, and H. Westerdahl, 2003, Sea bed logging (sbl), a new method for remote and direct identification of hydrocarbon filled layers in deepwater areas: First Break, **20**, 144–151.

Guptasarma, D., and B. Singh, 1997, New digital linear filters for hanke j0 and j1 transforms: Geophysical Prospecting, **45**, 83–89.

Hansen, K. R., and R. Mittet, 1975, Incorporating seismic horizons in inversion of csem data: Seg Houston 2009 International Exposition and Annual Meeting, Soc. Expl. Geophys., 694–698.

Key, K., 2009, 1d inversion of multicomponent, multifrequency marine csem data: Methodology and synthetic studies for resolving thin resistive layers: Geophysics, **74**, 9–20.

Kong, F. N., 2007, Hankel transform filters for dipole antenna radiation in a conductive medium: Geophysical Prospecting, **55**, 745–762.

Marquardt, D. W., 1962, An algorithm for least-squares estimation of nonlinear parameters: J. Soc. Indust. Appl. Math, **11**, 431–441.

Mittet, R., K. Brauti, H. Maulana, and T. A. Wicklund, 2008, Cmp inversion and post-inversion modelling for marine csem data: first break, **26**, 59–67.

Nabighian, M. N., 1987, Electromagnetic methods in applied geophysics-theory volume 1: Soc. of Expl. Geophys.

Tarantola, A., 2005, Inverse problem theory: Siam.

Tocantins, V. C. S., 2007, Modelagem numérica de dados mcsem 3d usando computação paralela: PhD thesis, Instituto de Geociências - Universidade Federal do Pará.

Um, E. S., and D. L. Alumbaugh, 2007, On the physics of the marine controlled-source electromagnetic method: Geophysics, **72**, WA13–WA26.

Vdeev, D. B., 2005, Three-dimensional electromagnetic modelling and inversion from theory to application: Survey in Geophysics, **26**, 767–799.

Zdhanov, M. S., 2001, Geophysical inverse theory and regularization problems: Elsevier.

——, 2009, Geophysical electromagnetical theory and methods: Elsevier.

Livros Grátis

(http://www.livrosgratis.com.br)

Milhares de Livros para Download:

Baixar livros de Administração
Baixar livros de Agronomia
Baixar livros de Arquitetura
Baixar livros de Artes
Baixar livros de Astronomia
Baixar livros de Biologia Geral
Baixar livros de Ciência da Computação
Baixar livros de Ciência da Informação
Baixar livros de Ciência Política
Baixar livros de Ciências da Saúde
Baixar livros de Comunicação
Baixar livros do Conselho Nacional de Educação - CNE
Baixar livros de Defesa civil
Baixar livros de Direito
Baixar livros de Direitos humanos
Baixar livros de Economia
Baixar livros de Economia Doméstica
Baixar livros de Educação
Baixar livros de Educação - Trânsito
Baixar livros de Educação Física
Baixar livros de Engenharia Aeroespacial
Baixar livros de Farmácia
Baixar livros de Filosofia
Baixar livros de Física
Baixar livros de Geociências
Baixar livros de Geografia
Baixar livros de História
Baixar livros de Línguas